crystals

MDPI

Article

Experimental Study of the Evolution of Creep-Resistant Steel's High-Temperature Oxidation Behavior

Gabriela Baranová [1], Mária Hagarová [1,*], Miloš Matvija [1], Dávid Csík [1,2], Vladimír Girman [3], Jozef Bednarčík [3,4] and Pavel Bekeč [5]

[1] Institute of Materials and Quality Engineering, Faculty of Materials, Metallurgy and Recycling, Technical University of Košice, Letná 9, 042 00 Košice, Slovakia; gabriela.baranova@tuke.sk (G.B.)
[2] Institute of Materials Research, Slovak Academy of Sciences, Watsonova 47, 040 01 Košice, Slovakia
[3] Institute of Physics, Faculty of Science, P. J. Šafárik University in Košice, Park Angelinum 9, 041 54 Košice, Slovakia
[4] Institute of Experimental Physics, Slovak Academy of Sciences, Watsonova 47, 040 01 Košice, Slovakia
[5] Železiarne Podbrezová Research and Development Centre, Ltd., Kolkáreň 35, 976 81 Podbrezová, Slovakia
* Correspondence: maria.hagarova@tuke.sk

Abstract: This study shows that in an atmosphere containing water vapor, the oxide layer on the surface of the 9CrNB steel MarBN (Martensitic 9Cr steel strengthened by Boron and MX Nitrides) was formed by an outer layer of hematite Fe_2O_3 and Cr_2O_3 and an inner two-phase layer of Fe_3O_4 and Fe_3O_4 + $(Fe, Cr)_2O_4$, which was confirmed by XRD analysis. Part of the layer consisted of nodules and pores that were formed during the increase in oxides when the present $H_2O(g)$ acted on the steel surface. The diffusion mechanism at temperatures of 600 and 650 °C and at longer oxidation times supported the "healing process" with a growing layer of Fe oxides and the presence of Cr and minor alloying elements. The effects of alloying elements were quantified using a concentration profile of the oxide layer based on quantitative SEM analysis, as well as an explanation of the mechanism influencing the structure and chemical composition of the oxide layer and the steel-matrix–oxide interface. In addition to Cr, for which the content reached the requirement of exceeding 7.0 wt. % in the inner oxide layer, W, Co, Mn, and Si were also found in increased concentrations, whether in the form of the present Fe-Cr spinel oxide or as part of a continuously distributed layer of Mn_2O_3 and SiO_2 oxides at the steel-matrix–oxide interface. After long-term high-temperature oxidation, coarser carbides of the $M_{23}C_6$ type (M = Fe,W) significantly depleted in Cr were formed at the oxide-layer/matrix interface. In the zone under the oxide layer, very fine particles of MC (M = V, Nb, and to a lesser extent also Cr in the particle lattice of the given phase) were observed, with a higher number of particles per unit area compared to the state before oxidation. This fact was a consequence of Cr diffusion to the steel surface through the subsurface zone.

Keywords: creep-resistant steel; high-temperature oxidation; oxide layer; oxidation kinetics; alloying elements

Citation: Baranová, G.; Hagarová, M.; Matvija, M.; Csík, D.; Girman, V.; Bednarčík, J.; Bekeč, P. Experimental Study of the Evolution of Creep-Resistant Steel's High-Temperature Oxidation Behavior. *Crystals* **2023**, *13*, 982. https://doi.org/10.3390/cryst13060982

Academic Editor: Petros Koutsoukos

Received: 4 May 2023
Revised: 31 May 2023
Accepted: 16 June 2023
Published: 20 June 2023

1. Introduction

Due to the nature of operating thermal equipment, superheater tubes are exposed to high temperature, which promotes an intense oxidation process [1–3]. The oxidation behavior of materials at high temperatures represents a very complex process of changes in their structure [4,5]. A serious problem resulting from rapid oxide growth on the surface is the reduction in heat transport and the ability of the superheater tube to resist high vapor pressures due to the material loss during oxidation. The steel's strength at high temperature becomes a major problem. Its reduced resistance to creep under harsh operating conditions (high temperature, high working medium pressure) limits the maximum application temperature of superheater materials [6,7].

For superheater tube production, 9–11Cr steels are used, for which sufficient creep strength, a low thermal expansion coefficient, good thermal conductivity, and resistance to high-temperature oxidation are required [3]. In general, the resistance of materials to high-temperature oxidation depends on Cr_2O_3-based oxides that are formed on the material surface during service and protect the steel from further degradation [8]. The increase in chromium oxides depends on outward diffusion of its cations, inward diffusion of oxygen, and diffusion along grain boundaries [9].

The utilization of 9Cr3W3CoVNbBN martensitic steel MarBN (Martensitic 9Cr steel strengthened by Boron and MX Nitrides) occurs in ultra-supercritical areas of heat power plants. As referenced in [10], these high-strength martensitic steels are applicable for temperature conditions up to 650 °C and steam pressure of 35 MPa. The elevated austenitization temperatures during standardized annealing create conditions for the dissolution of carbide, nitrides, and carbonitrides [11]. Study [11] specifies that steel tempering after standardized annealing results in higher microstructural stability, creating the needed durability when steel is exposed to long-term creep conditions. The composition of the steel microstructure consists of tempered martensite and bainite with carbides, mostly M 23 C 6 and finely dispersed MX-type precipitates (M = V, Nb, Cr; X = C, N).

Increasing the concentration of alloys in the alloy and/or reducing the grain size are alternatives for increasing oxidation resistance, as a protective chromium oxide layer can be formed that covers the steel matrix surface and prevents further oxidation [12–14]. Furthermore, the oxidation resistance of 9Cr steels can be significantly improved by addition of alloying elements. As found by the authors of [15], a continuous and stable oxide layer composed of Cr-rich oxides $(Fe,Cr)_2O_3$ and $MnCr_2O_4$ served as a protective barrier between the matrix and the environment at the early stage of oxide formation. The formation of Mn_2O_3 improved the oxide layer compacting. Silicon generally increases the resistance to oxidation. Amorphous SiO_2 forms at the oxide/matrix interface as a thin layer. The high affinity of Si for oxygen allows its increased occurrence even in the inner oxide layer [16]. As reported by the authors of [17] in 9Cr steels, the positive effect of Si stabilized at a value above about 0.5 wt. %. Study [18] focused on the oxidation of a group of steel grades containing approximately 11.5 wt. % Cr and different contents of Si, Mn, Mo, and W in air + $H_2O_{(g)}$ at higher temperatures. The authors state that there is a "common influence" of alloying elements on the magnitude of oxidation, where it can be assumed that steels with higher Si content (≈0.5 wt. %), high W content, and low Mo content form oxides with higher protective effect than steels with lower Si content, low W content, and high Mo content.

In assessing the influence of alloys, the authors of [19] concluded their work with a recommendation for steels operating in environments containing water vapor, namely, to replace part of the molybdenum with tungsten as a carbide-forming element to maintain creep strength. According to the authors, tungsten does not have a negative effect on the oxidation behavior of steels, manganese can help slow the rate of evaporation of chromium-containing volatile hydroxyl compounds, and silicon has a beneficial effect on slowing the rate of chromium depletion in the subsurface steel zone. This is how the prolongation of time to oxide breakaway is achieved. As reported by the authors of [20], apart from the decreasing oxide thickness, the most significant change in W alloying was the increased proportion of secondary phase at the oxide/matrix interface and also in the matrix.

The aim of this paper was to assess the influence of alloys and precipitating secondary phases on the high-temperature oxidation processes of 9Cr MarBN steel in humid environments. The aim was to describe their role in the mechanism of changes in the structure of the forming oxide layer, at the oxide/matrix interface, and in the matrix under the oxide layer during and after oxidation in a mixed atmosphere of air + 10% $H_2O_{(g)}$. The paper also aims to assess their influence on the resistance of 9Cr steels to high-temperature oxidation.

2. Materials and Methods

2.1. Material

First, 9Cr3W3CoVNbBN MarBN high-strength steel (Martensitic 9Cr steel strengthened by Boron and MX Nitrides) was selected as the experimental material. This steel contains boron and nitrogen, intended to precipitate fine particles of different types with a hardening and stabilizing effect on the martensitic matrix. The steel chemical composition is provided in Table 1.

Table 1. T Actual MarBN steel chemical composition.

Element	C	Mn	Si	P	S	Cr	Ni	Cu	Mo	V
wt. %	0.08	0.47	0.29	0.009	0.002	8.80	0.15	0.07	0.04	0.20
Element	W	Co	Al	Ti	Nb	B	As	Sn	N	B + N
wt. %	2.96	2.95	0.011	0.002	0.06	0.014	0.009	<0.01	0.0079	0.0219

The conclusive heat treatment of the MarBN steel ranged within the interval of 1060–1070 °C during standardized annealing and ultimately tempered at a range of 780–800 °C.

Oxidation test samples were derived from the provided 12.27 mm wall thickness tube, with a small-diameter hole near one edge needed to hang the samples in the furnace. All samples were ultra-sonically cleaned in acetone and dried prior to the experiment.

2.2. Methods

A horizontal laboratory furnace was utilized to create the conditions required to evaluate high-temperature steel oxidation. The main structures of the furnace consisted of the fuel supply, the high-temperature chamber, and an exhaust section. The application of distilled water to a horizontal retort created necessary atmospheric conditions for the experiment. A peristaltic pump was utilized to influence the atmospheric conditions by adjusting the automatic flow rate to 10% water vapor. Steel samples were hung in the high-temperature working chamber, and temperature was continuously monitored utilizing thermocouples. The reaction of the steel to the water vapor oxidation was evaluated at 600 °C and 650 °C for a duration of 3000 h.

The samples were taken from the furnace at the time periods of 500, 1000, 2000 and 3000 h.

The OLYMPUS VANOX-T light microscope was used for structural analysis of the as-delivered steel and the condition after long-term oxidation. Samples for microscopic analysis were prepared by standard metallographic procedures: grinding, polishing, and etching in Nital (2% HNO_3 in methanol). The morphology characterization and oxide layer composition were determined by the scanning electron microscope (SEM) JEOL JSM 7000F with energy-dispersive spectrometer. The oxidized layer phase composition was determined using X-ray diffraction with Rigaku Ultima IV equipment, with Cu Kα radiation (λ = 1.5406 Å) operated at 40 kV and 50 mA. The precipitation state of carbide and other phases in the steel before oxidation was analyzed by the JEOL JEM-2100F UHR transmission electron microscope (TEM) using the carbon extraction replica method. These were stripped from the metallographic prepared surfaces after separation in the Villela-Bain etchant. The chemical composition of each particle type was determined by EDS in the scanning transmission electron microscope (STEM) mode, and the phase analysis of the individual precipitate particles present in the provided steel substructure was carried out by means of selected-area electron diffraction (SAED) analysis with TEM. The substructure regions analyzed for steel samples were the longitudinal section regions, as in the case of metallographic analysis of their microstructure.

3. Results and Discussion

3.1. Microstructure of the MarBN Steel in the Initial State

The MarBN steel microstructure is documented in Figure 1. Observation shows that the microstructure is heterogeneous, formed by particles unevenly distributed in the steel matrix. Particles at the prior austenite grain boundaries, particles at the interfaces of the tempered martensite formations and within them, particles in the tempered bainite formations, and also relatively fine particles around and within these formations were observed.

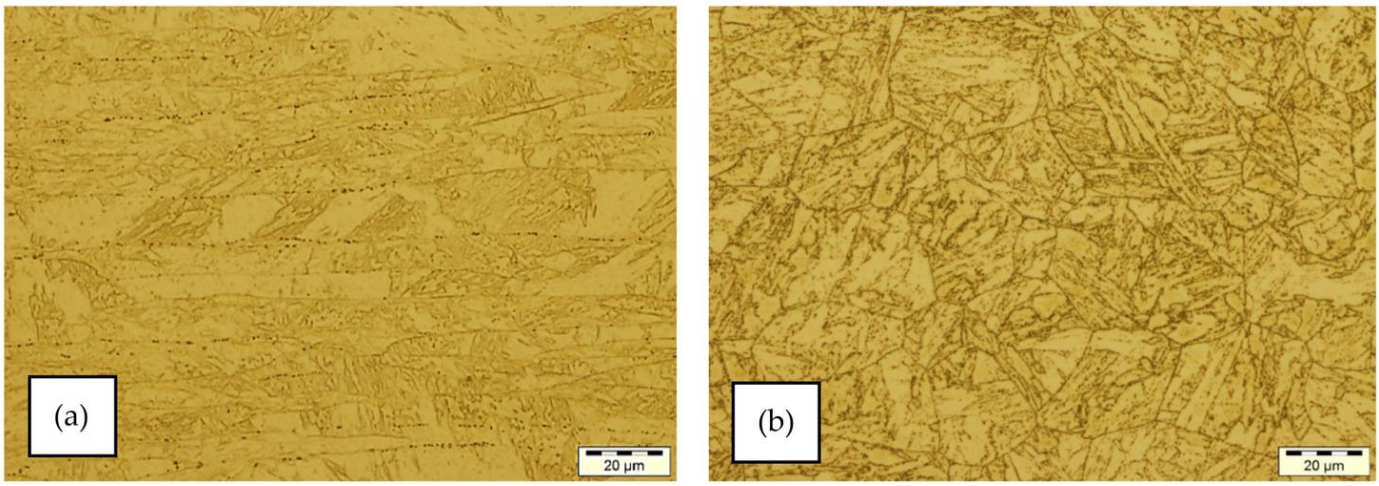

Figure 1. MarBN steel microstructure: (**a**) after rolling and before standardization annealing and tempering, (**b**) after standardization annealing and tempering, LM, etch.

The microstructure after rolling was formed by martensitic and bainitic laths, which were formed in the prior austenite grains. The laths of martensite and bainite were uniformly distributed and had different orientations in different regions of the microstructure. Prior austenitic grain boundaries were also observed in the microstructure, on which oval particles of precipitates were locally excluded. These particles were often arranged in rows that were related to the original austenite grain boundaries. A small amount of smaller oval precipitate particles were found inside the bainitic and martensitic laths and at their interfaces.

The morphology of the microstructure after normalizing annealing and tempering appeared homogeneous at lower magnification. It was a needle-like morphology with particles of precipitates. The microstructure consisted of tempered martensite and tempered bainite. In the smaller regions of the evaluated microstructure, they were mostly parallel-oriented. The observed bainitic laths had a considerably larger width compared to the martensitic laths. Darker and lighter areas were visible in the slatted morphology of the microstructure, which was the result of inhomogeneous redistribution of precipitate particles. A more detailed study of the microstructure showed that at the interfaces of the needles, there were fine particles of precipitates. In light areas of the microstructure, the proportion of particles was smaller, and in darker areas, it was higher. The nature of the exclusion of these probable carbide particles was thus influenced by the differences in the morphology of the needles between the laths of tempered martensite and lower bainite. Their exclusion also occurred during tempering at the prior austenite grain boundaries, which accentuated these boundaries. In areas with narrow and short martensite laths, the distribution of carbide particles is more homogeneous than in areas with thicker and longer martensite laths.

TEM Analysis of MarBN Steel in the Initial State

Figure 2a,b exhibit the microstructure of the steel at its initial state prior to exposure to the atmospheric oxidation conditions documented by TEM. Upon evaluation, the

microstructure was determined to be mixed and heterogeneous. Formations consisted of tempered martensite and tempered bainite, as well as precipitate particles of varying morphology, size, and non-standardized distribution in the steel structure, at different morphological formations, at the boundaries of relatively coarse prior austenite grains, at the tempered martensite and tempered bainite formation interfaces, and within these formations. The process of standardization steel annealing influenced the distribution and nature of tempered martensite due to the nature of martensite laths as well as bainite formations of the tempered bainite. Additionally, studies [21,22] evaluated the standardization annealing process and structure of 9–11Cr martensitic steels.

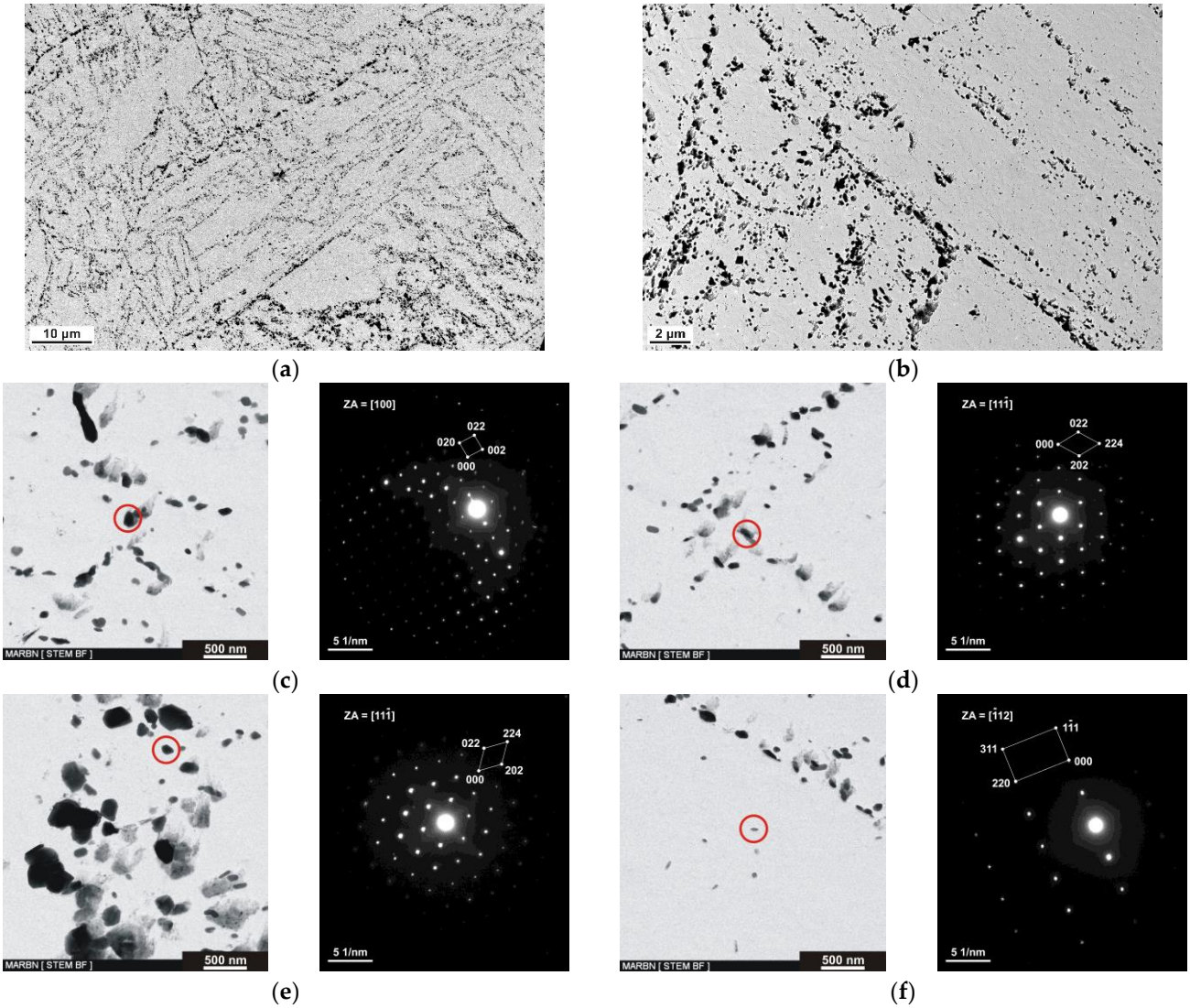

Figure 2. Particles morphology and distribution in the microstructure of initial steel state (**a**,**b**). Particles present in the area of prior austenite grain boundaries (**c**); particles present in the area of tempered martensite (**d**); particles present in the area of tempered bainite (**e**); and present particles in steel substructure (**f**), with SAED pattern and corresponding phase analysis. The red circles on the bright field images (**c**–**f**) mark the area corresponding to the SAED.

Figure 2c shows the results of SAED analysis of particles present at and around the prior austenitic grain boundaries, which, according to the EDS analyses results, contained, in addition to a high C content, mostly Cr, a slightly lower Fe content, W, and in some cases a minor V content. The SAED results show that the particles in question represent complex $M_{23}C_6$-type carbides crystallizing in a face-centered cubic lattice (FCC, S.G. 225).

Hence, these are $M_{23}C_6$-type carbides with possible mutual substitution of Cr, Fe, W, and V atoms in the lattice of phase particles. The steel substructure analysis showed that particles in the steel substructure were particles with oval, rod-like, and globular morphologies located inside the tempered martensite and tempered bainite formations and at their interfaces, which are the result of steel tempering. In addition to C, the particles present in the tempered martensite regions had a high Cr content, lower Fe and W contents, and a minor V content. Based on the diffraction analysis results, the particles were also identified as complex carbides of the $M_{23}C_6$ type with possible substitution of Cr, Fe, W, and V atoms in the lattice of the given phase. The particles present in the tempered bainite regions' formations had a high Cr content, in addition to C, and lower Fe and W contents. These particles were also determined by diffraction analysis to be complex $M_{23}C_6$ carbides with possible inter-substitution of Cr, Fe and W atoms in the lattice of the phase. The particles present in the tempered bainite regions' formations had high Cr and lower Fe and W contents in addition to C. These particles were also determined to be complex $M_{23}C_6$ carbides with possible mutual substitution of Cr, Fe, and W atoms in the lattice of the given phase based on the diffraction analysis results. Very fine globular particles with a relatively uniform distribution were also present in the steel substructure in the initial state. According to the EDS analyses results, they contained a high content of Nb and a lower content of V in addition to C. Based on SAED analysis, the given particles were identified as NbC crystallizing particles in a face-centered cubic lattice (FCC, S.G. 225), for which substitution of Nb and V atoms is possible. In the study [23], the precipitates Fe- and Cr-rich MX carbides and Fe-rich M_3C carbides were identified using TEM analysis.

3.2. Oxide Layer Morphology and Identification of MarBN Steel after Oxidation at 600 °C

The cross-section of the oxidized steel after 500, 1000, and 3000 h of oxidation at 600 °C in an oxidizing mixed atmosphere of air +10% H_2O(g) is shown in Figure 3.

On the steel surface, after 500 h of oxidation at 600 °C, there was a thin uneven oxide layer with a thickness of about 7–10 µm (Figure 3a). At the interface between the outer and inner oxide layers, a discontinuously distributed relatively high number of voids was visible. The formation of voids in the oxides can be explained by the transport mechanism of water vapor molecules through the oxide layers [24,25]. The oxygen transport towards the steel surface is facilitated specifically by H_2O. At higher water vapor concentrations, a large number of voids is created by the $CrO_2(OH)_2$ oxide formation. At the same time, diffusion along voids takes place (outer oxide layer), which is faster than diffusion along interstitial sites (inner oxide layer). This was investigated, e.g., in the work of the authors of [26–28]. The boundary between the inner and outer layer, visible in Figure 3a, represented the original steel surface. The inner oxide layer grew as part of the original surface and formed a segmented interface with the steel matrix.

With increasing oxidation time, it was possible to observe a change in the thickness and morphology of the outer and inner oxide layers on the steel. After 1000 h of oxidation at 600 °C (Figure 3c), the outer layer had a greater thickness, about 15–20 µm. Compared to the outer layer formed after 500 h of oxidation, it was more compact and more evenly distributed on the surface. The amount and size of the voids, which were already forming isolated areas, especially at the interface between the outer and inner oxide layers, were also reduced. The interface between the inner oxide layer and the steel matrix was more uniform. As the authors of [29] stated in their work, the formation of the inner oxide layer, which is crucial in protecting the base metal, is due to the internal oxidation. It is generally assumed that the outer oxide layer grows outward by diffusion of Fe cations through the inner and outer oxide layers to the outer-oxide-layer/matrix interface, while the inner oxide layer grows inward by diffusion of oxygen through the outer and inner oxide layers to the inner-oxide-layer/matrix interface [29,30].

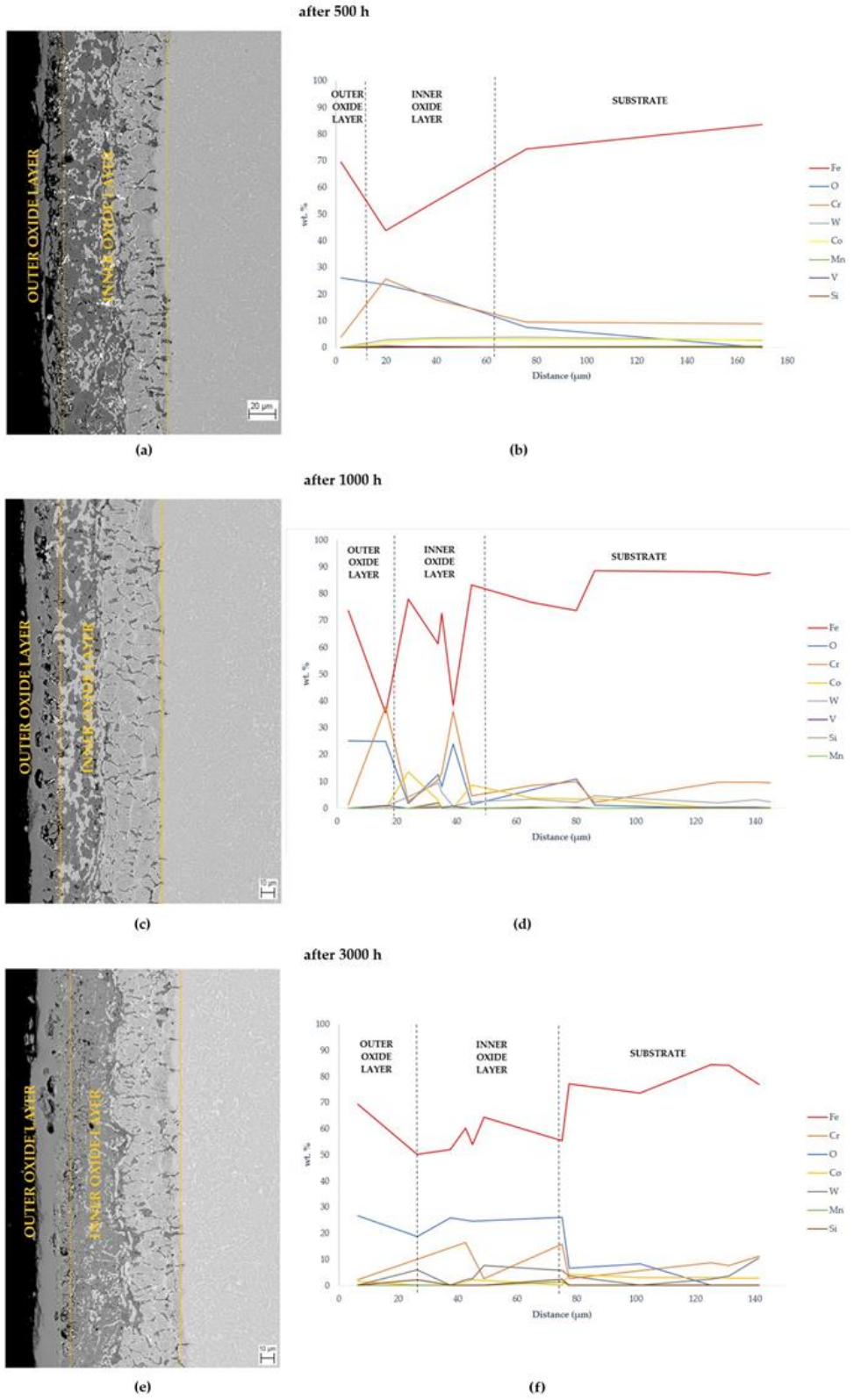

Figure 3. Cross-section of the oxidized steel with concentration profiles of analyzed elements across the oxide layer at temperature 600 °C after (**a**,**b**) 500 h, (**c**,**d**) 1000 h, (**e**,**f**) 3000 h oxidation, SEM.

After 3000 h of steel oxidation at 600 °C, the outer oxide layer thickness increased to a maximum of about 25 μm (Figure 3e). The layer was compact and covered the surface quite uniformly. Voids at the interface of the outer and inner layers were sporadic and were isolated embedded in the oxide layer. As stated by the authors of [30], it is likely that void

closure may have occurred, due to re-oxidation. The inner oxide layer at the steel interface produced morphology with larger protrusions into steel.

Concentration profiles of the analyzed elements obtained by processing the quantitative EDS SEM analysis (Figure 3b,d,f) showed the mechanism of oxide layer saturation from the steel side. After 500 h of oxidation, mainly Fe and Cr oxides were present in the outer oxide layer, with the Cr content being above about 3 wt. %. At the interface of the outer and inner oxide layer, Cr was above 25 wt. %, probably as a part of the carbides in the steel. The inner layer of Fe oxides was enriched with elements diffusing from the steel: Cr, Co, W, and Mn. As it was a part of the steel original surface, the content of Cr, W, or Co in some places corresponded to carbides or carbon nitride of mentioned elements in the microstructure of creep-resistant steel.

The Si occurrence was mainly visible at the interface between the inner oxide layer and the steel matrix (Figure 3b).

The inner layer of Fe oxides was enriched in elements diffusing from the steel. As it was part of the original steel surface, the Cr, W, or V content in some places corresponded to carbides or carbonitrides of these elements in the heat-resistant steel microstructure. After 1000 h of oxidation, Cr content in the outer layer decreased to a level above about 1.4 wt. % (Figure 3d). In the inner layer of Fe oxides, the redistribution of elements occurred during diffusion. The Cr content was very different; in some areas, it corresponded to Cr oxide at a level of more than 4.0 wt. %, while in other places, it could be found in complex FeCr-based oxides with a content of about 20 wt. %. The content of Co, W, and Mn was lower with the increasing thickness of this layer. The content of V varied by tenths of wt. %. The highest concentration of Si remained at the inner-oxide-layer/matrix interface.

The elements diffusion from steel and oxygen diffusion into steel continued during 3000 h of oxidation (Figure 3f). According to the authors of [31], the outer layer grew at the oxide/atmosphere interface due to the transport of Fe ions through the oxide and the Cr-rich oxide grew at the oxide/matrix interface due to internal oxygen transport.

The Cr-rich inner layer was also identified in other 9Cr steels, e.g., in the works of [9,12,32]. The steel oxidation mechanism was also described by the authors of [29] in their work. They specified that both outward Fe ions diffusion as well as inward oxygen diffusion also took place along the grain boundaries. After prolonged exposure, the internal oxides' size increased and new oxides were formed deeper in the matrix. As reported by the authors of [33], the inner oxide layer with the presence of the Cr-enriched spinel layer formed during oxidation slowed down further diffusion of cations and anions. As a result, the 9Cr steel was highly resistant to high-temperature oxidation. While the Cr content in the outer oxide layer dropped to approx. 2.0 wt. %, at the outer and inner oxide layers' interface, the Cr content was around 16 wt. %, which is a prerequisite for its presence in FeCr spinel. The content of Co, W, and V was increased at the interface of the outer and inner layer of oxides. The content of Mn and Si was increased mainly at the interface of the inner oxide layer with the matrix.

3.2.1. EDS SEM Maps of MarBN Steel Oxide Layer after Oxidation at 600 °C

To determine the elements distribution in the oxide layer at the earlier oxidation stages after 500 h and at the end of oxidation after 3000 h, the EDS SEM analysis was performed across oxidized samples, the outcome of which was EDS maps of the analyzed elements' distribution, shown in Figures 4a–h and 5a–h.

The outer and inner oxide layers were rich in Fe after 500 h of oxidation (Figure 4b). Chromium was detected in higher concentration in the inner layer, and the outer layer was more depleted of this element (Figure 4d). This was confirmed by the Cr concentration profile across the oxide layer (Figure 3b).

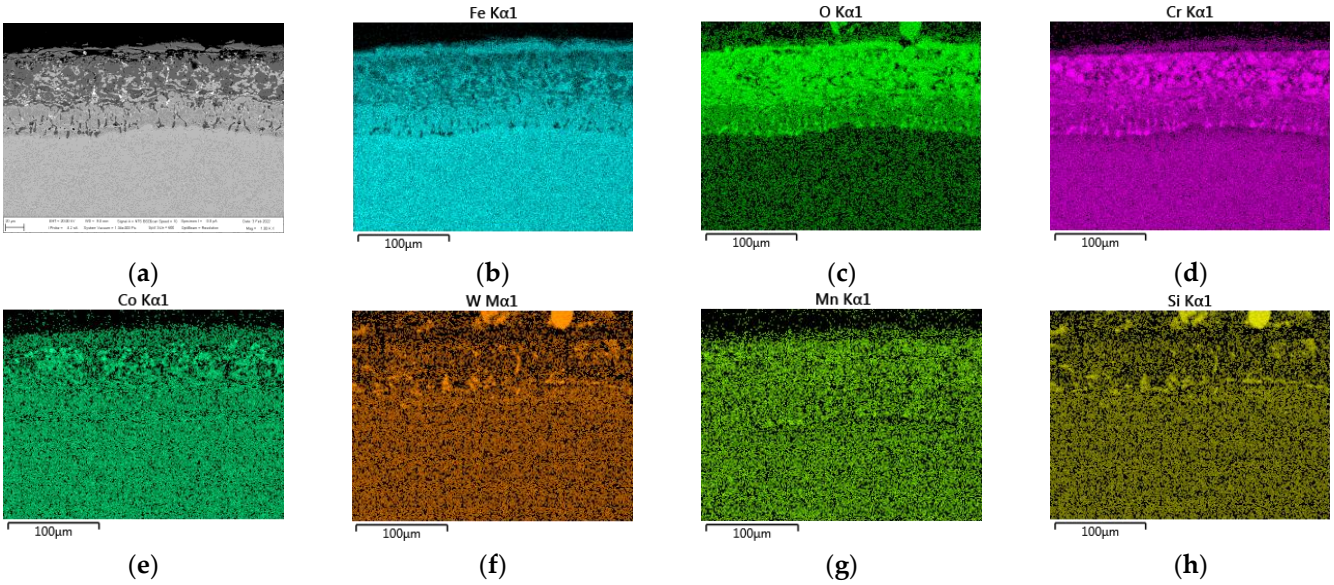

Figure 4. EDS maps of analyzed elements distribution after 500 h of oxidation at 600 °C.

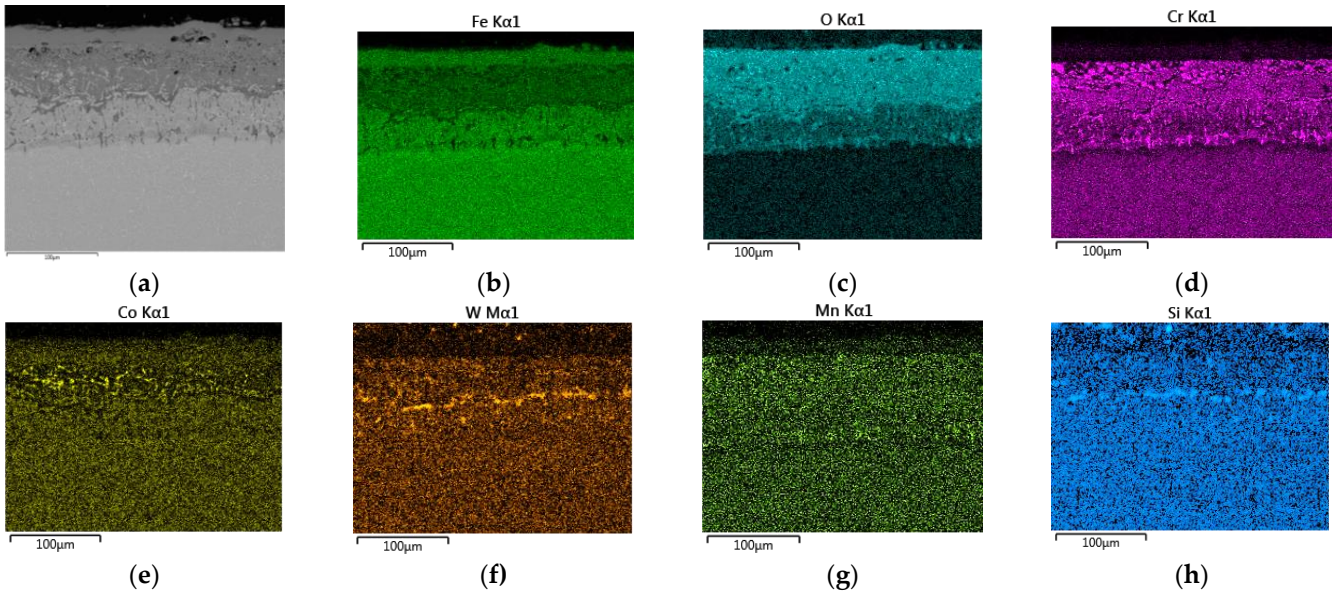

Figure 5. EDS maps of analyzed elements distribution after 3000 h of oxidation at 600 °C.

This suggests a mechanism of Cr oxide formations that were produced by the oxidation of Cr-rich carbides (deposited prior to oxidation along martensite/bainite plate boundaries and at the prior austenite grain boundaries in the steel structure). During high-temperature oxidation, they became part of $FeCr_2O_4$ and Cr_2O_3 [34]. The Fe and Cr distribution maps (Figure 4b,d) were complementary: the Cr-rich regions were depleted of Fe, and vice versa. The oxygen map showed its increased content at the location of Cr-enriched zones. Similar reasoning was also described in [9,35]. The inner oxide layer was mainly enriched in cobalt (Figure 4e). The silicon effect was achieved due to its diffusion into steel surface and SiO_2 formation on its surface (Figure 4h). After 500 h of oxidation, the highest proportion of the W-rich secondary phase was concentrated at the oxide/matrix interface, which can be seen by the brightest places in Figure 4f.

After 3000 h of exposure, the microstructure evolution during oxidation at a given temperature of 600 °C varied with the amount of Cr, with a sharper interface formed by the brightest places with the highest Cr concentration in the inner oxide layer and also at the interface of the inner and outer oxide layers (Figure 5d). In the oxidation process on

the SiO_2 layer (Figure 5h), chromium oxide was formed during 3000 h of oxidation. The oxygen activity, thermodynamically induced by SiO_2, was too small to form iron oxide layers. Hence, as might be expected from the thermodynamics described in more detail by the authors of [36] in their paper, the Si oxide formed a relatively compact layer beneath the chromium oxide in the inner oxide layer. This distribution was confirmed by EDS SEM analysis of both elements in Figure 5d,h. Tungsten, after 3000 h of oxidation, formed a more continuous distribution at the inner-oxide-layer/matrix interface (Figure 5f). Similarly, Si distribution changed with oxidation time. Its bright regions in Figure 5h indicated a higher concentration at the inner-oxide-layer/matrix interface [20]. Furthermore, the authors of [37] confirmed that long-term oxidation resulted in stable Si oxides' formation and their segregation at the oxide/metal-matrix interface.

Oxide growth is determined by affinity to oxygen and diffusion of alloying elements. According to [38], the Gibbs free energy of formation of all Mn-oxides is more negative than that of Fe-oxides, and the Gibbs free energy of formation of MnO and Mn-Cr spinel is even more negative than that of Cr_2O_3. This statement was also supported, e.g., by the authors of [39]. As they stated in their work, Mn-Cr spinel oxides are probably formed by the reaction of $MnO + Cr_2O_3 \rightarrow MnCr_2O_4$. Therefore, the presence of Mn in the oxide layer should increase the oxides' stability. Thus, Mn can be expected to be preferentially concentrated in the oxides at the oxide/matrix interface in the early stage of oxidation [40], as was confirmed in our study (Figures 3f and 5g).

3.2.2. XRD Phase Analysis of the Oxide Layer at 600 °C

In order to investigate the oxidation products of MarBN steel after 3000 h of oxidation at 600 °C, the steel was analyzed cross-sectionally by XRD diffraction. As shown in Figure 5, the oxide layer was formed mainly by Fe and Cr oxides. The main phases of the oxide layer were hematite, Cr_2O_3, and magnetite. By combining the data from the XRD record with the EDS SEM analyses, it was possible to identify Fe-Cr spinel even though the spectrum of $(Fe,Cr)_3O_4$ completely coincided with the XRD spectrum of magnetite. The results of the study [41] were similar and indicate diffraction peaks of Cr_2O_3, Fe_3O_4, and Fe_2O_3. The sequence of formed oxide layers was also found by [42].

However, taking into account the results shown in Figure 6, it is clear that the main phases of the outer oxide layers are hematite and magnetite [41].

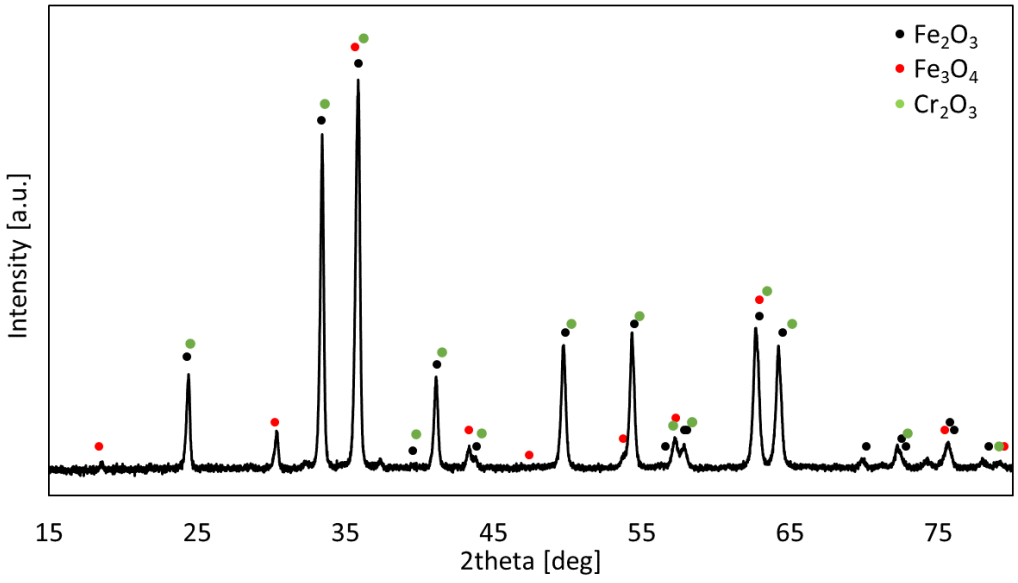

Figure 6. XRD phase analysis of the MarBN steel oxide layer after oxidation at 600 °C.

3.3. Morphology and Identification of the Oxide Layer on MarBN Steel after Oxidation at 650 °C

The surface of 9Cr3W3CoVNbBN steel after 500 h of oxidation at 650 °C in an air environment with 10% water vapor is shown in Figure 7a. An oxide layer with a thickness of 15–20 µm was formed on the surface. This layer was fairly uniform and compact, but it formed a separate interface from the inner layer with the occurrence of voids in a fairly continuous linear arrangement. The arrangement of voids was also discussed by the authors of [43].

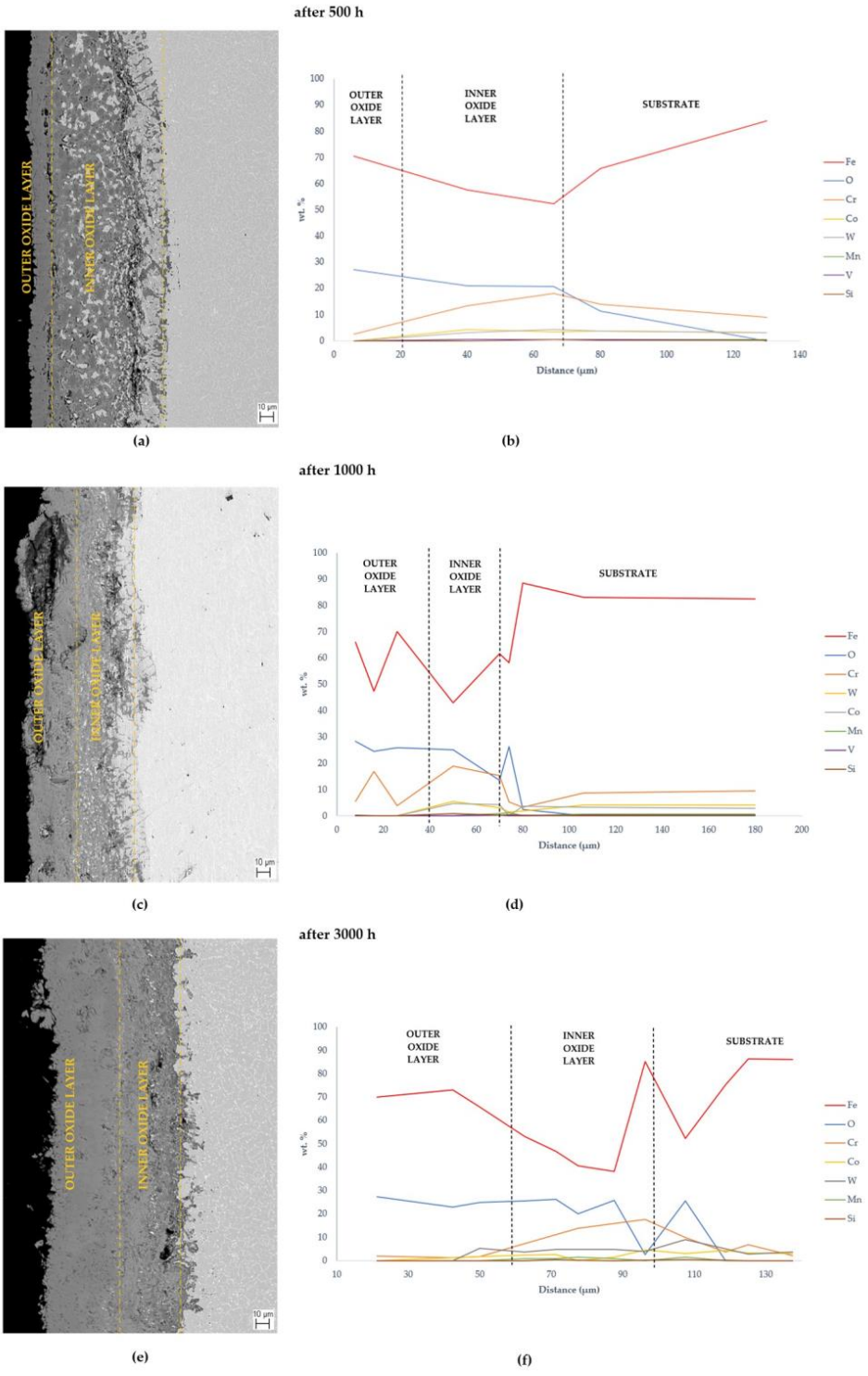

Figure 7. Cross-section of the oxidized steel with concentration profiles of analyzed elements across the oxide layer at temperature 650 °C after (**a**,**b**) 500 h, (**c**,**d**) 1000 h, (**e**,**f**) 3000 h oxidation, SEM.

Furthermore, the paper concluded that voids have the highest tendency for crack nucleation. Compared to void spacing, void size induces higher impact on the oxide cracking tendency. As stated by the authors of [30], for the iron–chromium system where breakaway oxidation occurs, the resulting layer microstructure contains many voids, and spallation is also common.

The inner oxide layer reached a thickness of about 60–70 µm. It was formed during the oxidation process as part of the original steel surface. The interface with the steel matrix was not as significantly separated as in the case of the outer and inner layers but also largely consisted of voids defining the oxide/matrix interface.

At the start of the oxidation process, the internal oxygen diffusion is rapid due to thin oxide layers.

At this time, internal oxidation can easily occur inside the grain and explains well the formation of Cr-rich oxide [44]. As the paper further states, the oxidation of grain boundaries/laths of martensite and bainite and the formation of Cr-rich oxides inside the grain contribute to the inner oxide layer's growth at an early stage. After 1000 h of steel oxidation at 650 °C due to diffusion processes, the thickness of the outer layer increased to about 40 µm (Figure 7c), with the highest concentration of voids remaining at the original interface of the outer and inner layer, as it was observed after 500 h of oxidation (Figure 7a). The authors of [45] describe that in a closed furnace space, thermodynamic equilibrium is reached at the oxide/matrix and oxide/atmosphere interfaces, which determines oxide growth by diffusion of reactants through the oxide layer. Metal cations and oxygen anions tended to migrate through the oxide layer in opposite directions. As can be seen in Figure 7c, the interface between the inner oxide layer and the matrix was not sharply separated; still, it had a more structured morphology.

After 3000 h of the MarBN steel oxidation at 650 °C, an outer compact oxide layer with a thickness of about 60 µm was formed on the surface (Figure 7e). The occurrence of voids at the outer and inner oxide layers' interface was rare. Higher void concentration was found at the inner-oxide-layer/matrix interface. Several papers confirmed void presence at this interface [9,42,46].

The concentration profile of the analyzed elements after the cross-section after 500 h of oxidation showed that the outer layer mainly contained Fe oxides and a proportion of Cr at the level of max. 2.7 wt. % (Figure 7b). At the interface of the outer and inner layers of oxides, the concentration of Cr was found at the level of its presence in carbides. The inner oxide layer consisted mainly of Fe oxides and Cr. The layer also contained W and Co, which were part of the original steel surface. Si and Mn were mainly located at the oxide/matrix interface.

After 1000 h of oxidation, diffuse redistribution of the analyzed elements took place: in the outer oxide layer, the Cr content was above about 5.0 wt. %, and in the inner layer, Cr was part of the oxide layer in the form of oxides with a content of about 4.0 wt. % or part of FeCr spinel with a content above 20.0 wt. % (Figure 7d). Other analyzed elements Co and W were found in the inner oxide layer and at the oxide-layer/matrix interface in concentrations corresponding to their content in the steel or as part of carbides and carbonitrides. The distribution of Si and Mn was mainly at the oxide/matrix interface.

After 3000 h of oxidation, Cr content in the outer layer was lower than after shorter exposure times, ranging from 1.2 to 1.9 wt. % (Figure 7f). In the inner oxide layer, the Cr content was at a level corresponding to that in spinel, i.e., above 14.0 wt. %. The content of Co, W, and V corresponded to their content in the steel. A higher W content was recorded as part of the carbides, not only in the inner oxide layer but also at the oxide/matrix interface. At the inner oxide layer and matrix's interface, Fe oxides were analyzed, and high Cr content of about 18.0 wt. %, Co content of more than 4.0 wt. %, W content of 4.0 wt. % and above, and V content in tenths of wt. % were detected. The distribution of Si and Mn remained at the oxide/matrix interface.

3.3.1. EDS SEM Maps at 650 °C

The distribution maps of analyzed elements show that with increasing exposure time of MarBN steel in a mixed furnace atmosphere at 650 °C, regions with higher concentration of alloying elements with protective anti-oxidation effect were formed (Figure 8a–h).

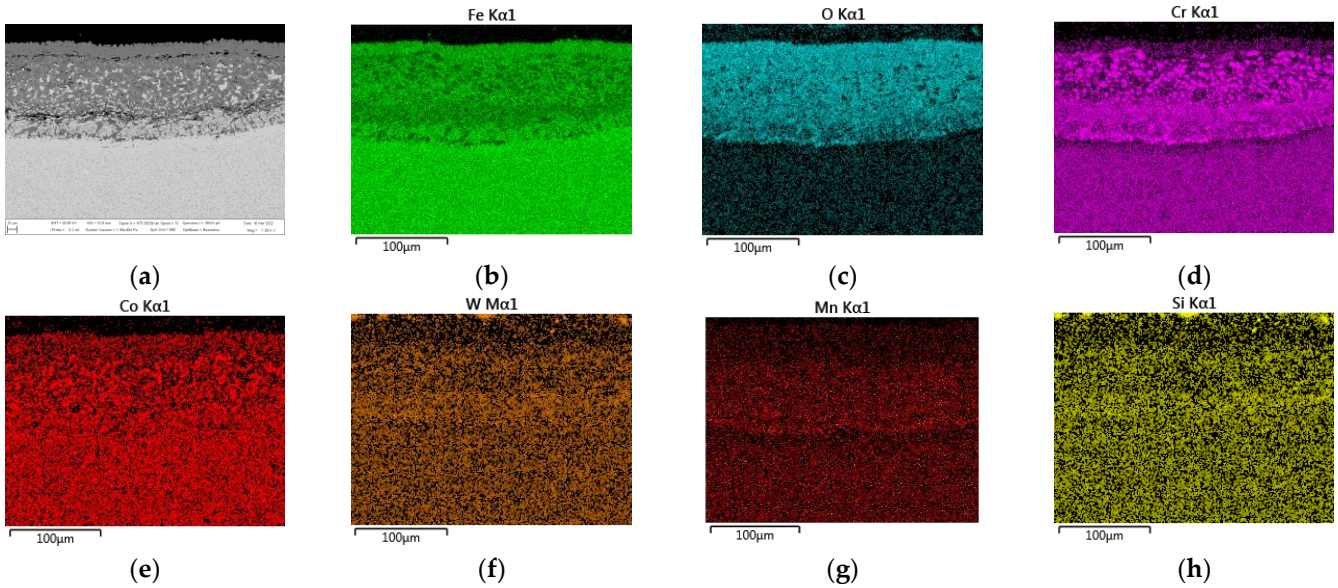

Figure 8. EDS distribution maps of analyzed elements after 500 h of oxidation at 650 °C.

After 500 h of exposure, the formed outer oxide layer contained mainly Fe oxides with a small proportion of Cr oxides (Figure 8b,d). The oxide layer and matrix's interface with higher proportions of W, Mn and Si was formed (Figure 8f–h). Higher Co concentration was identified in the inner oxide layer (Figure 8e).

After 3000 h of high-temperature oxidation in the alloyed 9Cr3W3CoVNbBN steel, an inner layer mainly rich in Cr, Mn, and Si was formed, with the highest concentration at the inner-oxide-layer/matrix interface (Figure 9a–h). W concentration in the inner oxide layer and at the oxide-layer/matrix interface increased (Figure 9f).

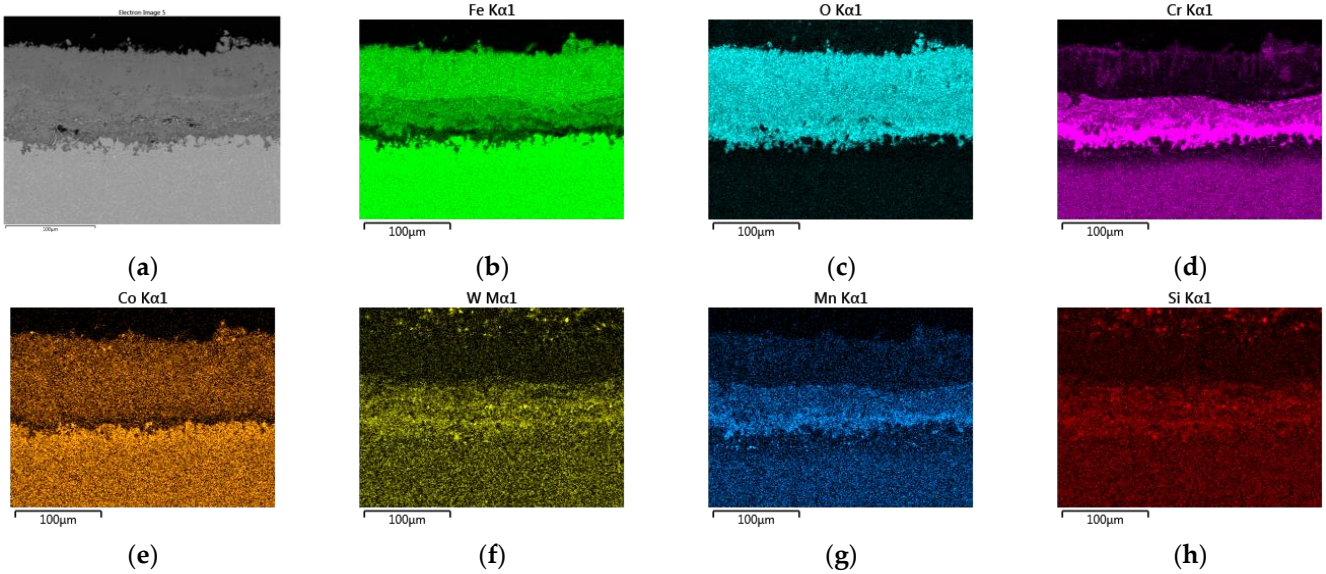

Figure 9. EDS distribution maps of analyzed elements after 3000 h of oxidation at 650 °C.

It is an assumption that this Cr-rich layer formation is the result of transition from internal to external oxidation, where the outward Cr diffusion rate exceeds the inward oxygen diffusion rate. When the oxide is sufficiently dense, it significantly slows down the oxygen diffusion inward, as stated by the authors of [44] in the conclusions of their work. As the authors of [44] stated in their paper, Cr-rich oxide precipitates were the result of preferential oxidation along the grain boundaries and laths of martensite, while the latter were the result of internal oxidation. As further analyzed by the authors of that work, the inner oxide layer consisted of Cr in Cr-rich spinel oxide surrounded by Fe-rich spinel oxide. The formation of such a composite oxide layer was also reported in our study.

3.3.2. XRD Phase Analysis of the Oxide Layer at 650 °C

To identify the phases present in the oxidation products, an XRD analysis was also performed on the oxidized surface of the MarBN steel after 3000 h exposure in a mixed environment at a temperature of 650 °C (Figure 10). The result shows the presence of Fe oxides (hematite and magnetite), Cr oxides, and a minor proportion of Co oxide. The main oxide phase detected by XRD analysis was hematite and Cr oxide together with magnetite. In the case of an oxidation temperature of 650 °C, Co oxide was identified. As the authors stated in the paper [47] concerning the different intensity of diffraction peaks in XRD patterns, it was found that the oxidation of the materials was accelerated with the increase in experimental temperature.

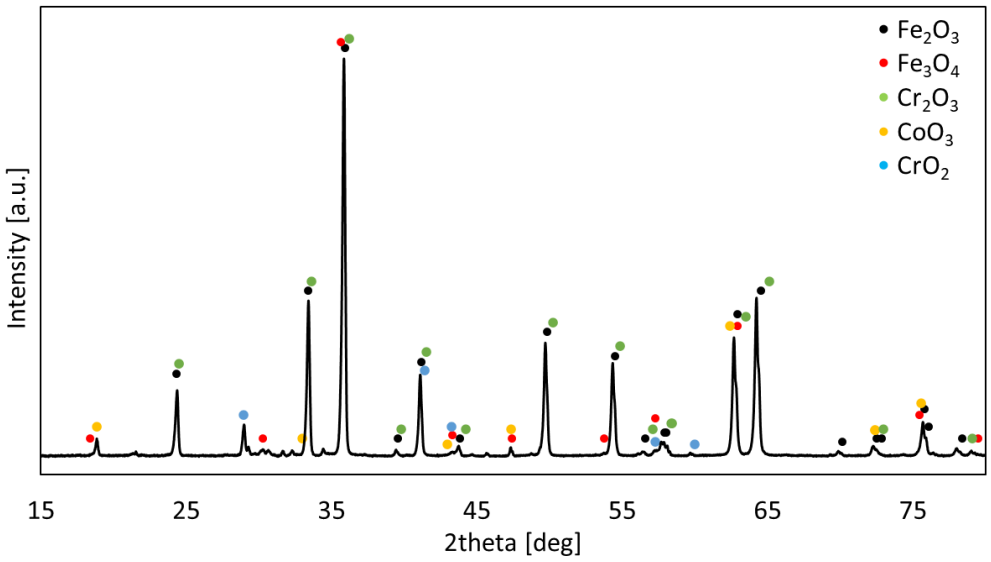

Figure 10. XRD phase analysis of the MarBN steel oxide layer after oxidation at 650 °C.

3.3.3. TEM Analysis of MarBN Steel after Oxidation at 650 °C

The steel microstructure's nature after exposure to the oxidizing furnace atmosphere at 650 °C for 3000 h is obvious from Figure 11a,b. In the region below the oxide layer formed, a zone with a markedly different distribution and arrangement of particles present is visible. Coarser particles were observed there without any indication of their typical arrangement like in the rest of the steel microstructure. By assessing the nature and chemical nature of these particles based on EDS analysis, it was shown that they contained a high content of C with a majority of Fe and W and a significantly lower Cr content compared to the particles below this zone. This fact indicates that the particles were significantly depleted in Cr due to diffusion into the oxide layer on the steel surface during the oxidation process (at 650 °C during 3000 h). As the authors of the study [34] stated, the increase in Cr-enriched oxides on the steel surface is accompanied by their decrease in the matrix and the growth in the particle size in the area at the oxide/matrix interface. Based on SAED results (Figure 11c), it can be argued that these are particles of complex carbides of the $M_{23}C_6$ type crystallizing

in a face-centered cubic lattice with possible mutual substitution of Fe, W, and, to a minor extent, Cr atoms in the lattice of particles of the given phase. Very fine particles with high regional number of particles per unit area were also observed in the given zone just below the oxidized surface. This, according to results of EDS analysis, contained a high proportion of C with a majority of V and also Nb, as well as a minority of Cr. Based on SAED results, it can be argued that these are VC phase particles crystallizing in a cubic lattice (S.G. 196) with possible mutual substitution of V, Nb, and minority Cr atoms in the lattice of particles of the given phase. Similar results of EDS, SEM, and TEM analyzes of oxidized 9–12Cr F-M steel substructure were also declared in the study [48]. The authors stated that there was a zone of Cr depletion under the oxide layer. As the authors further state, this promoted the enrichment of Cr into the layer by growing oxides. Cr-rich precipitates were present immediately below the Cr-depletion zone in the matrix.

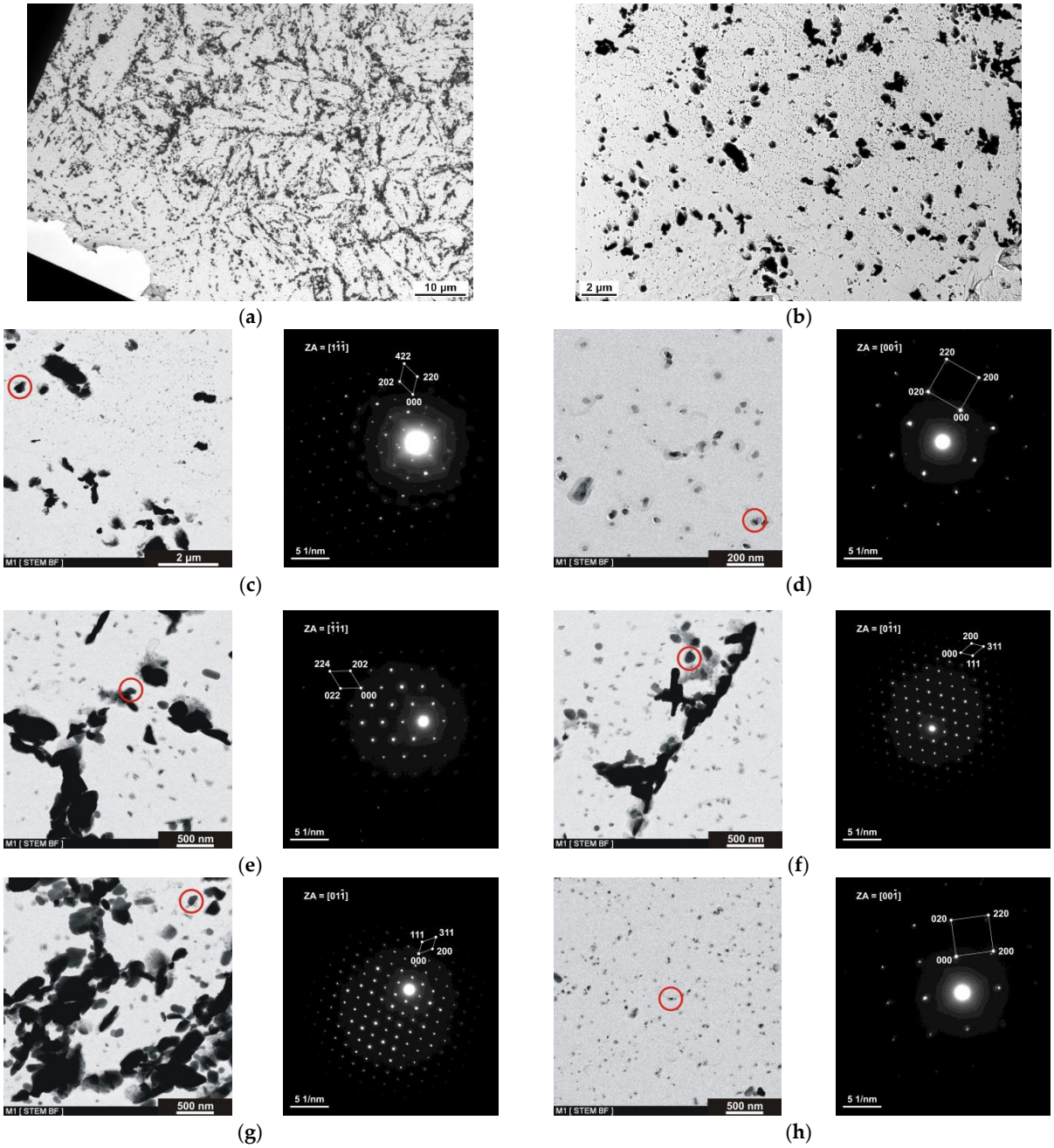

Figure 11. (**a**,**b**) Particles morphology and distribution in the microstructure of steel after exposure to the oxidizing furnace atmosphere (650 °C for 3000 h). (**c**) Coarse particles present in the zone under

the oxide layer; (**d**) thin particles present in the zone under the oxide layer; (**e**) particles present in the area of prior austenite grain boundaries; (**f**) particles present in the area of tempered martensite; (**g**) particles present in the area of tempered bainite; and (**h**) present particles in steel substructure with SAED pattern and corresponding phase analysis. The red circles on the bright field images (**c**–**f**) mark the area corresponding to the SAED.

The steel structure's nature in the region below the zone showed a very similar character to the initial state of analyzed steel, with a typical arrangement of particles at the boundaries of the relatively coarse prior austenite grains, at the tempered martensite and tempered bainite formations interfaces, and within these formations. The particles present at and around the prior austenitic grain boundaries, according to EDS analyses results, contained, in addition to a high C content, a major Fe and Cr content, a slightly lower W content, and a minor V content. The SAED results showed that particles represent complex carbides of the $M_{23}C_6$ type with possible mutual substitution of Fe, Cr, W, and V atoms in the lattice of particles of the given phase. The particles located in the tempered martensite regions contained, in addition to C, high Cr and lower Fe and W contents. Based on SAED results, the particles were also identified as $M_{23}C_6$-type complex carbides, with possible substitution of Cr, Fe, and W atoms in the lattice of the given phase. The particles present in the tempered bainite regions formations had high Cr and lower Fe and W contents in addition to C. These particles were determined to be complex $M_{23}C_6$ carbides with possible mutual substitution of Cr, Fe, and W atoms in the lattice of the given phase based on the diffraction analysis results. Very fine globular particles with a relatively uniform distribution with high contents of both C and V and lower contents of Nb and Cr were also observed in the steel substructure. By electron diffraction analysis, the particles were identified as VC crystallizing particles in a cubic lattice with possible substitution of V atoms by other alloying elements, mainly Nb and Cr. Fine particles in the steel state after exposure to oxidation process in the reaction atmosphere showed a greater presence of Cr compared to the initial state, which was due to its diffusion from the coarser carbide particles towards the steel surface through the subsurface zone and simultaneous formation of fine particles that showed a higher regional number of particles per unit area compared to the initial state.

4. Conclusions

The 9Cr3W3CoVNbBN MarBN steel (Martensitic 9Cr steel strengthened by Boron and MX Nitrides) was oxidized at 600 and 650 °C for 3000 h in a mixed atmosphere of air + 10% H_2O and characterized by SEM, TEM and XRD analyses. In this study, the mechanisms leading to the improvement of resistance to high-temperature oxidation were understood by using modern electron microscopic analyses. These were supplemented by XRD analysis to detect the phases in the oxide layer.

The results and their discussion in this work led to the following conclusions:

- The microstructure of MarBN steel after normalizing annealing and tempering consisted of tempered martensite and tempered bainite with particles of carbide-based precipitates.
- An oxide layer was formed on the surface of the MarBN martensitic–bainitic steel, which consisted of the outer layer formed by Fe_2O_3 with Cr_2O_3 presence and the inner oxide layer formed by Fe_3O_4 and spinel Fe-Cr.
- EDS SEM analysis showed the importance of the alloys' transport into the forming oxide layer during long-term exposure. Chromium, as the main alloying element, was essential in the inner oxide layer during the Fe-Cr spinel formation. Mn and Si were important in the passive layer of oxide formation at the oxide/matrix interface already in the earlier stages of oxidation, and during long-term oxidation, their effect only increased during long-term oxidation.
- By XRD analysis, Fe_2O_3, Cr_2O_3, and Fe_3O_4 phases were identified in the oxide layer after 3000 h of oxidation at a temperature of 600 °C, whereas Fe_2O_3, Cr_2O_3, CrO_2,

Fe_3O_4, and CoO_3 were identified at a temperature of 650 °C. By combining the data from the XRD record with EDS SEM analysis, it was possible to identify Fe-Cr spinel, which together with Fe_3O_4 created an effective barrier against further oxidation.

- TEM analysis from the zone under the oxide layer showed coarser particles of complex carbides of the $M_{23}C_6$ type (M = Fe, W) significantly depleted of Cr due to its diffusion into the oxide layer on the steel surface during the oxidation process.
- In the zone under the oxide layer, very fine particles with a high number of particles per unit area were also observed, which, according to the results of the EDS analysis, contained a high proportion of C with a majority content of V and Nb and a minor Cr content. Diffusion of Cr was directed from the coarser carbide particles from the surface of the steel through the subsurface zone by the formation of fine particles.
- Under the indicated zone, the steel structure's nature was very similar to the initial state of the analyzed steel.
- The entire described process leads to the result that 9Cr heat-resistant steels have a high resistance to high-temperature oxidation due to the formation of spinel enriched with alloys in the inner oxide layer, supported by passivation by Si oxides at the oxide/matrix interface. The strength properties of the steel remain preserved due to the presence of fine stable carbides V and Nb and due to the structure at a distance from the oxide layer, which preserves the character of the original structure.

Author Contributions: Conceptualization, G.B. and M.H.; methodology, G.B. and M.H.; validation, G.B., M.H., M.M. and D.C.; formal analysis, G.B., M.H., M.M., D.C., V.G., J.B. and P.B.; investigation, G.B., M.M., D.C. and J.B.; resources, M.H. and P.B.; data curation, G.B. and M.H.; writing—original draft preparation, G.B., M.H. and M.M.; writing—review and editing, G.B., M.H., M.M., D.C. and V.G.; visualization, G.B., M.M. and D.C.; supervision, M.H.; project administration, G.B.; funding acquisition, V.G. All authors have read and agreed to the published version of the manuscript.

Funding: This research was funded by a grant of the Scientific Grant Agency grant number VEGA 1/0406/20.

Institutional Review Board Statement: Not applicable.

Informed Consent Statement: Not applicable.

Data Availability Statement: All data are available upon reasonable request from the corresponding author.

Acknowledgments: The research described in this paper was financially supported by the Scientific Grant Agency—the grant project VEGA 1/0406/20.

Conflicts of Interest: The authors declare no conflict of interest.

References

1. Ardy, H.; Bangun, D.A. Failure Analysis of Superheater Boiler Tube SA 213 T12. *IOP Conf. Ser. Mater. Sci. Eng.* **2019**, *547*, 012035. [CrossRef]
2. Zhang, T.; Zhang, X.; Bayar, N.; Zhao, Z. Review of oxide scale on high temperature heating surface in boiler. *IOP Conf. Ser. Earth Environ. Sci.* **2021**, *692*, 022049. [CrossRef]
3. Sun, K.; Wang, J.; Yan, Y.; Jiang, J.; Deng, L. Failure Analysis of Tube-Burst on T91 Platen Superheater of 600 MW Supercritical Boiler. In Proceedings of the International Conference on Artificial Intelligence and Electromechanical Automation (AIEA), Tianjin, China, 26–28 June 2020; pp. 453–456. [CrossRef]
4. Yu, C.; Zhang, J.; Young, D.J. High temperature corrosion of Fe-Cr-(Mn/Si) alloys in CO_2-H_2O-SO_2 gases. *Corros. Sci.* **2016**, *112*, 214–225. [CrossRef]
5. Wang, S.; Zheng, Z.; Zheng, K.; Long, J.; Wang, J.; Ren, Y.; Li, Y. High temperature oxidation behavior of heat resistant steel with rare earth element Ce. *Mater. Res. Express.* **2020**, *7*, 016571. [CrossRef]
6. Dudziak, T.; Łukaszewicz, M.; Simms, N.; Nicholls, J. Analysis of High Temperature Steam Oxidation of Superheater Steels Used in Coal Fired Boilers. *Oxid. Met.* **2015**, *85*, 171–187. [CrossRef]
7. Gupta, G.K.; Chattopadhyaya, S. Critical Failure Analysis of Superheater Tubes of Coal-Based Boiler. *J. Mech. Eng.* **2017**, *63*, 287–299. [CrossRef]

8. Meier, G.H.; Jung, K.; Mu, N.; Yanar, N.M.; Pettit, F.S.; Abella´n, J.P.; Olszewski, T.; Hierro, L.N.; Quadakkers, W.J.; Holcomb, G.R. Effect of Alloy Composition and Exposure Conditions on the Selective Oxidation Behavior of Ferritic Fe-Cr and Fe-Cr-X Alloys. *Oxid. Met.* **2010**, *74*, 319–340. [CrossRef]
9. Zhong, X.; Wu, X.; Han, E. The characteristic of oxide scales on T91 tube after long-term service in an ultra-supercritical coal power plant. *J. Supercrit. Fluids* **2012**, *72*, 68–77. [CrossRef]
10. Abe, F. Research and Development of Heat-Resistant Materials for Advanced USC Power Plants with Steam Temperatures of 700 °C and Above. *Engineering* **2015**, *1*, 211–224. [CrossRef]
11. Dudova, N.; Mishnev, R.; Kaibyshev, R. Effect of Tempering on Microstructure and Mechanical Properties of Boron Containing 10%Cr Steel. *ISIJ Int.* **2011**, *51*, 1912–1918. [CrossRef]
12. Wu, Q.; Liu, Y.; Zhang, Z.; Qi, Y.; Zhang, C.; Zheng, H.; Xu, Y. Oxidation behavior and high-temperature tensile properties of Fe-9Cr-(Mo, Mo/Ni) alloys. *Corros. Sci.* **2021**, *181*, 109243. [CrossRef]
13. Ma, H.; He, Y.; Liu, Y.; Shin, K. Effects of precipitation on the scale and grain growth in 9% Cr tempered martensite steel upon steam oxidation. *Mater. Charact.* **2020**, *167*, 110497. [CrossRef]
14. Hagarová, M.; Vaško, M.; Pástor, M.; Baranová, G.; Matvija, M. Effect of Flue Gases' Corrosive Components on the Degradation Process of Evaporator Tubes. *Materials* **2021**, *14*, 3860. [CrossRef] [PubMed]
15. Chen, S.; Jin, X.; Rong, L. Improvement in High Temperature Oxidation Resistance of 9%Cr Ferritic–Martensitic Steel by Enhanced Diffusion of Mn. *Oxid. Met.* **2015**, *85*, 189–203. [CrossRef]
16. Ishitsuka, T.; Inoue, Y.; Ogawa, H. Effect of Silicon on the Steam Oxidation Resistance of a 9%Cr Heat Resistant Steel. *Oxid. Met.* **2004**, *61*, 125–142. [CrossRef]
17. Ennis, P.; Quadakkers, W.J. The steam oxidation resistance of 9-12% chromium steels, in materials for advanced power generation. *Energy Technol.* **2002**, *21*, 1131–1142.
18. Lepingle, V.; Louis, G.; Allué, D.; Lefebvre, B.; Vandenberghe, B. Steam oxidation resistance of new 12%Cr steels: Comparison with some other ferritic steels. *Corros. Sci.* **2008**, *50*, 1011–1019. [CrossRef]
19. Schütze, M.; Schorr, M.; Renusch, D.P.; Donchev, A.; Vossen, J.P.T. The role of alloy composition, environment and stresses for the oxidation resistance of modern 9% Cr steels for fossil power stations. *Mater. Res.* **2004**, *7*, 111–123. [CrossRef]
20. Kang, J.-Y.; Ha, H.-Y.; Kim, S.-D.; Park, J.Y.; Jang, M.-H.; Lee, T.-H. Effect of tungsten on the oxidation of alumina-forming austenitic stainless steel. *Appl. Microsc.* **2019**, *49*, 13. [CrossRef]
21. Dudova, N. 9–12% Cr Heat-Resistant Martensitic Steels with Increased Boron and Decreased Nitrogen Contents. *Metals* **2022**, *12*, 1119. [CrossRef]
22. Yan, P.; Liu, Z.; Bao, H.; Weng, Y.; Liu, W. Effect of normalizing temperature on the strength of 9Cr–3W–3Co martensitic heat resistant steel. *Mater. Sci. Eng. A* **2014**, *597*, 148–156. [CrossRef]
23. Cai, Y.; Wang, Q.; Liu, M.; Jiang, Y.; Zou, T.; Wang, Y.; Li, Q.; Pei, Y.; Zhang, H.; Liu, Y.; et al. Tensile Behavior, Constitutive Model, and Deformation Mechanisms of MarBN Steel at Various Temperatures and Strain Rates. *Materials* **2022**, *15*, 8745. [CrossRef] [PubMed]
24. Chandra-ambhorn, S.; Nilsonthi, T.; Wexternals, Y.; Galerie, A. Oxidation of simulated recycled steels with 0.23 and 1.03 wt.% Si in Ar-20%H_2O at 900 °C. *Corros. Sci.* **2014**, *87*, 101–110. [CrossRef]
25. Hagarová, M.; Baranová, G.; Fujda, M.; Matvija, M.; Horňak, P.; Bednarčík, J.; Yudina, D. High Temperature Oxidation Behavior of Creep Resistant Steels in Water Vapour Containing Environments. *Materials* **2022**, *15*, 616. [CrossRef]
26. Naraparaju, R. High Temperature Oxidation Behaviour of Boiler Steels with Emphasis on Shot-Peening Effects—Experimental Results and Simulation. Ph.D. Thesis, Universität Siegen, Siegen, Germany, 2013.
27. Li, Y.; Macdonald, D.D.; Yang, J.; Qiu, J.; Wang, S. Point defect model for the corrosion of steels in supercritical water: Part I, film growth kinetics. *Corros. Sci.* **2019**, *163*, 108280. [CrossRef]
28. Li, Y.; Xu, T.; Wang, S.; Fekete, B.; Yang, J.; Yang, J.; Qiu, J.; Xu, A.; Wang, J.; Xu, Y.; et al. Modelling and Analysis of the Corrosion Characteristics of Ferritic-Martensitic Steels in Supercritical Water. *Materials* **2019**, *12*, 409. [CrossRef]
29. Shen, Z.; Tweddle, D.; Yu, H.; He, G.; Varambhia, A.; Karamched, P.; Hofmann, F.; Wilkinson, A.J.; Moody, M.P.; Zhang, L.; et al. Microstructural understanding of the oxidation of an austenitic stainless steel in high-temperature steam through advanced characterization. *Acta Mater.* **2020**, *194*, 321–336. [CrossRef]
30. Saunders, S.R.J.; Monteiro, M.; Rizzo, F. The oxidation behaviour of metals and alloys at high temperatures in atmospheres containing water vapour: A review. *Prog. Mater. Sci.* **2008**, *53*, 775–837. [CrossRef]
31. Quadakkers, W.J.; Ennis, P.J.; Zurek, J.; Michalik, M. Steam oxidation of ferritic steels—Laboratory test kinetic data. *Mater. High Temp.* **2005**, *22*, 47–60. [CrossRef]
32. Yan, J.-J.; Huang, X.-F.; Huang, W.-G. High-temperature oxidation behavior of 9Cr-5Si-3Al ferritic heat-resistant steel. *Int. J. Miner. Metall. Mater.* **2020**, *27*, 1244–1250. [CrossRef]
33. Chen, Y.; Sridharan, K.; Ukai, S.; Allen, T.R. Oxidation of 9Cr oxide dispersion strengthened steel exposed in supercritical water. *J. Nucl. Mater.* **2007**, *371*, 118–128. [CrossRef]
34. Gheno, T.; Monceau, D.; Young, D.J. Mechanism of breakaway oxidation of Fe-Cr and Fe-Cr-Ni alloys in dry and wet carbon dioxide. *Corros. Sci.* **2012**, *64*, 222–233. [CrossRef]
35. Bischoff, J.; Motta, A.T.; Comstock, R.J. Evolution of the oxide structure of 9CrODS steel exposed to supercritical water. *J. Nucl. Mater.* **2009**, *392*, 272–279. [CrossRef]

36. Huntz, A.M.; Bague, V.; Beauplé, G.; Haut, C.; Sévérac, C.; Lecour, P.; Longaygue, X.; Ropital, F. Effect of silicon on the oxidation resistance of 9% Cr steels. *Appl. Surf. Sci.* **2003**, *207*, 255–275. [CrossRef]
37. Zhang, Y.; Zou, D.; Li, Y.; Wang, Y.; Zhang, W.; Zhang, X. Effect of Al content on the high-temperature oxidation behavior of 18Cr–Al–Si ferritic heat-resistant stainless steel. *J. Mater. Res. Technol.* **2021**, *11*, 1730–1740. [CrossRef]
38. Jung, I.-H. Critical evaluation and thermodynamic modeling of the Mn-Cr-O system for the oxidation of SOFC interconnect. *Solid State Ion.* **2006**, *177*, 765–777. [CrossRef]
39. Srinivasan, S.; Mallika, C.; Krishna, N.G.; Thinaharan, C.; Jayakumar, T.; Kamachi Mudali, U. Evolution of surface chemistry and morphology of oxide scale formed during initial stage oxidation of modified 9Cr–1Mo steel. *Corros. Sci.* **2014**, *79*, 59–68. [CrossRef]
40. England, D.M.; Virkar, A.V. Oxidation Kinetics of Some Nickel-Based Superalloy Foils and Electronic Resistance of the Oxide Scale Formed in Air Part, I. *J. Electrochem. Soc.* **1999**, *146*, 3196. [CrossRef]
41. Laverde, D.; Gómez-Acebo, T.; Castro, F. Continuous and cyclic oxidation of T91 ferritic steel under steam. *Corros. Sci.* **2004**, *46*, 613–631. [CrossRef]
42. Mathiazhagan, P.; Khanna, A.S. High Temperature Oxidation Behavior of P91, P92 and E911 Alloy Steels in Dry and Wet Atmospheres. *High Temp. Mater. Process.* **2011**, *30*, 43–50. [CrossRef]
43. Yan, J.; Qiu, Y.; Da, B.; Li, Z.; Li, Y.; Ding, Z.; Ma, L.; Zhang, P.; Yuan, Y.; Gu, Y. Impact of the voids on the cracking behavior of the duplex oxide scale on the 18%Cr austenite alloy surface. *Corros. Sci.* **2020**, *163*, 108298. [CrossRef]
44. Chen, K.; Zhang, L.; Shen, Z. Understanding the surface oxide evolution of T91 ferritic-martensitic steel in supercritical water through advanced characterization. *Acta Mater.* **2020**, *194*, 156–167. [CrossRef]
45. Abellán, J.P.; Olszewski, T.; Meier, G.H.; Singheisera, L.; Quadakkers, W.J. The oxidation behaviour of the 9% Cr steel P92 in CO_2 and H_2O-rich gases relevant to oxyfuel environments. *Int. J. Mater. Res.* **2010**, *101*, 287–299. [CrossRef]
46. Demizieux, M.-C.; Desgranges, C.; Martinelli, L.; Favergeon, J.; Ginestar, K. Morphology and Buckling of the Oxide Scale after Fe-9Cr Steel Oxidation in Water Vapor Environment. *Oxid. Met.* **2019**, *91*, 191–212. [CrossRef]
47. Bao, Z.; Han, R.; Zhu, Y.; Li, H.; Li, N.; Tang, M.; Zhang, H.; Zhao, C. High Temperature Oxidation Behavior of New Martensitic Heat-Resistant Steel. *Mater. Sci.* **2022**, *28*, 164–170. [CrossRef]
48. Oleksak, R.P.; Addou, R.; Gwalani, B.; Baltrus, J.P.; Liu, T.; Trey Diulus, J.; Devaraj, A.; Herman, G.S.; Doğan, Ö.N. Molecular-scale investigation of the oxidation behavior of chromia-forming alloys in high-temperature CO_2. *NPJ Mater. Degrad.* **2021**, *5*, 46. [CrossRef]